



Dynamic thermo-mechanical coupling and size effects in finite shape memory alloy nanostructures

R.P. Dhote^{a,b,*}, R.V.N. Melnik^{b,c}, J. Zu^a

^a Department of Mechanical and Industrial Engineering, University of Toronto, 5 King's College Road, Toronto, ON, Canada M5S3G8

^b M²NeT Laboratory, Wilfrid Laurier University, Waterloo, ON, Canada N2L3C5

^c Ikerbasque, Basque Foundation for Science and BCAM, 48011 Bilbao, Spain

ARTICLE INFO

Article history:

Received 19 October 2011

Received in revised form 29 March 2012

Accepted 24 May 2012

Keywords:

Shape memory effects

Thermo-mechanical coupling

Nanowires

Phase transformation

Twinning

Finite element method

Microstructures

ABSTRACT

In this paper, the dynamics of martensitic transformations in shape memory alloy (SMA) constrained finite nanostructures is studied using a phase field model with the Ginzburg–Landau free energy. The nonlinear coupled thermo-mechanical properties in SMAs have been extensively studied in the bulk case. However at the nanoscale the thermal physics has been usually neglected in a study of SMA properties, and most of the model developments have been carried out under the assumption of isothermal phase transformations. The main aim of this paper is to develop a model that couples the thermal physics and the mechanical dynamics to study the influence of such coupling on the mechanical properties of SMA nanostructures. The developed model is solved using the finite element method. Analyzing FePd alloy nanowires, we observe a steeper slope of the stress–strain curve in the coupled thermo-mechanical case due to temperature evolution during the loading–unloading cycle of such nanostructures. We also observe the martensitic suppression phenomenon in constrained nanowires and nanograins on cooling. We have developed a semi-analytical model to predict a critical size at the onset of martensitic suppression. The semi-analytical model predicts a critical size which is in a good agreement with the numerical results for FePd nanograins.

© 2012 Elsevier B.V. All rights reserved.

1. Introduction

Shape memory alloys (SMAs) possess important characteristics of shape recovery upon thermal and mechanical loading. Such shape recovering characteristics give rise to two complex behaviors known as shape memory effect and superelasticity. These behaviors differ in a way the SMA specimen can recover its shape at the end of the loading–unloading cycle. Both these behaviors are hysteretic, highly non-linear and strongly temperature dependent. They have been studied extensively in the literature (see e.g. books by Lagoudas [1], Bhaatacharya [2], etc.).

SMAs exhibit their properties due to the underlying phenomenon of martensitic transformations (MT) [2]. The MT is a first order solid-to-solid diffusionless phase transformation (PT) from the high temperature austenite phase to the low temperature martensite phases or between martensite phases. MTs are caused due to atomic rearrangements, with movement of atom less than an atomic distance, with an instantaneous strain. The austenite and

martensite phases differ in their atomic arrangements by distortion or dimension change. These phases are elastically accommodated to produce complex microstructures to minimize the energy.

Several modeling approaches have been used to describe the hysteretic behavior and mechanical properties of SMAs. An extensive review of the models are found in [1,3,4]. Phase field (PF) models have emerged as a powerful computational approach for modeling microstructures of ferroelectric [5–9] and ferroelastic systems [10–14]. This approach has a unified framework that describes stress and temperature induced phase transformations in the variational nature of the model. The PF models have been used largely to study microstructures and mechanical properties of meso- and nano-scale SMA specimens.

Bouville and Ahluwalia [15] used the PF model to study the effect of size and shape on the microstructure evolution and the mechanical properties of martensite in the case of constrained nanostructures. Ahluwalia et al. [14] investigated the effect of strain loadings on the microstructure evolution and its influence on mechanical properties of 3D cubic-to-tetragonal PTs in nano-scale samples. Idesman et al. [16] studied the effect of inertial forces on the microstructure evolution in 2D and 3D PTs using the advanced dynamic formulation developed by Levitas and Preston [17]. All the above studies reviewed so far, have been limited to the SMA nanostructure behaviors accounting for the structural (or

* Corresponding author at: Department of Mechanical and Industrial Engineering, University of Toronto, 5 King's College Road, Toronto, ON, Canada M5S3G8. Tel.: +1 4169463709; fax: +1 4169787753.

E-mail address: rakesh.dhote@utoronto.ca (R.P. Dhote).

mechanical) dynamics (or uncoupled structural physics) only, under a strong hypothesis of isothermal phase transformations.

The isothermal hypothesis is valid in the environment where temperature is carefully controlled (e.g. for a SMA specimen in air-flow with high velocity) and loading is quasi-static, allowing heat transfer to the environment. Pieczyska et al. [18–20] experimentally studied the temperature evolution in SMA specimen surface subjected to dynamic loading–unloading using infrared thermography. They observed temperature increase–decrease during loading–unloading of the SMA specimen. The temperature variation influence on the stress–strain behavior of the material was clearly demonstrated. The stress–strain curves during phase transformations become steeper in the environment without temperature control (the coupled thermo-mechanical case) compared to the temperature controlled environment (isothermal conditions, the uncoupled case) during the dynamic loading.

The isothermal hypothesis in the PF models [14,15] puts some limitations on getting further insight into the inherent thermo-mechanical properties in SMAs. The importance of coupled thermo-mechanical effects in modeling has recently been demonstrated also for low dimensional nanostructures by Melnik and Mahapatra [21]. So far, there has been a very limited discussion about the coupled thermo-mechanical behavior of SMA nanostructures. For a better understanding of the dynamics of phase transformations in SMA structures at the nanoscale, the coupled thermo-mechanical effects need to be accounted in the modeling. In this work, we use a computationally inexpensive low dimensional model developed in our earlier work for the mesoscale [22,23] and extend it to study the microstructure and mechanical properties of finite size SMA nanostructures.

The novel property of MT suppression has been observed in SMA nanostructures below a critical dimension (or size) on cooling. This phenomenon has been confirmed earlier by experimental observations [24] and numerical simulations [15,25]. The knowledge of impact of crystal size on the martensitic PT is crucial for engineering purposes. Several models have been reported to predict the critical size in SMAs (e.g. [26] and references therein). Porta et al. [27] showed the dependence of MT suppression phenomenon on the elastic free energy, temperature and size of the martensite domain within an austenite host matrix. Waitz et al. [24] analytically calculated the critical size in the NiTi nanograins by accounting the transformation barrier due to chemical and mechanical driving forces. Eliseev and Morozovska [28] proposed a general analytical approach for the description of size effects in ferroelectric nanosystems based on the variational method and the Landau–Ginzburg–Devonshire (LGD) phenomenology. In this work, we develop a semi-analytical model to predict the critical size in square SMA nanograins based on the LGD phenomenology.

The rest of the paper is organized as follows. In Section 2, we present a general mathematical framework for modeling the dynamics of SMA and develop a coupled thermo-mechanical model for 2D square-to-rectangular PTs. The development of a semi-analytical model for predicting the critical size of SMA nanostructures on cooling is described in Section 3. Section 4 describes the numerical experiments carried out on FePd SMA nanowires and nanograins using the coupled thermo-mechanical model developed in Section 2. Finally, Section 5 provides conclusions and discuss a scope for future work.

2. Mathematical model for SMA dynamics

The mechanical properties of SMAs are dependent on the microstructures of austenite and martensite phases and their combinations. The mathematical framework for modeling microstructures

can be described by a variational problem [2,29,30]. The total energy of a SMA specimen in reference configuration Ω , subjected to deformation Y at a temperature θ is given by

$$W(Y) = \int_t \int_{\Omega} \varphi(Y, \theta) dV dt, \quad (1)$$

where $\varphi(Y, \theta)$ is the non-convex free energy function, t is time, and V is the volume. The microstructures correspond to the minimization of Eq. (1) [31]. Using appropriate boundary conditions, the energy of the structure can be minimized over the whole domain. This procedure in general case may produce infinitely many minimizers and extremely fine twins, thus raising several difficulties mentioned in the literature [29,30,32]. In solving Eq. (1), there are several numerical challenges connected with local minima, resulting from phase mixtures under low and moderate temperature regimes, and non-convexity of the problem [29,30,33]. These problems can be solved with a more precise definition of the free energy by incorporating the strain gradient energy terms that maintain the finite twins in a domain. In this paper, we construct a mathematical model for the simulation of microstructures and mechanical properties in SMAs on the basis of the phase field (PF) model and the LGD theory.

2.1. Mathematical model formulation on the basis of the Landau–Ginzburg–Devonshire theory

The PF models have been used in the past to study the microstructures and mechanical properties of SMA nanostructures [14,15,34,35]. In the PF model, the SMA dynamics is described by modeling the appropriate free energy \mathcal{F} of the PT. As the SMA is a first order solid-to-solid PT, it is described with a good approximation by the phenomenological Landau theory. The Landau theory leads to a coarse-grained model of the PT phenomenon under the assumption that an average order parameter (OP) (OP distinguishes different phases in the domain) must be small as compared to OP itself [36]. The theory expresses the free energy in a polynomial expansion of average OPs using the lattice dynamics, elasticity theory, and group theory. The free energy is based on the symmetry change of a crystallographic PTs [37].

In PF models, the order parameter is used to differentiate different phases in a domain. The strains are used to describe different phases in the SMA domain [38]. The strains, which directly contribute to the phase transformation are called OPs, and the others are called as non-OPs (nop). The free energy \mathcal{F} is derived on the basis of symmetric strain tensor [32,38]. A generalized form of the free energy \mathcal{F} is written as

$$\mathcal{F} = \mathcal{F}_{\text{op}} + \mathcal{F}_{\text{nop}} + \mathcal{F}_{\text{gradient}}, \quad (2)$$

where \mathcal{F}_{op} is the energy part due to the OPs, which contributes to MT as per the Landau–Devonshire theory, \mathcal{F}_{nop} is the energy part due to non-OPs, which contributes to the bulk and shear energy, and $\mathcal{F}_{\text{gradient}}$ is the gradient energy which contributes to the energy cost required for maintaining different phase domains in a structure and interface formed between physical boundaries and domain. The gradient energy term (or Ginzburg energy) maintains a non-zero width in austenite–martensite and martensite–martensite interfaces, and prevents the system from creating an infinite number of interfaces [29]. This term also introduces the nanoscale length in the PF model [15,36,39,40]. The $\mathcal{F}_{\text{gradient}}$ can be mathematically split into the surface and volume energy terms by using the divergence theorem. The surface energy is analogous to the surface tension in the superconducting and magnetic films. In the bulk systems, the surface energy is often neglected because of the periodic boundary conditions or negligible variation of OP at the surface for larger length scales. However, the effect of surface energy becomes increasingly important in a finite size nanosystem [36]. The LGD theory has been applied previously to nanoferroelastic

and nanoferroelectric systems to study the dynamic behavior of nanostructures [15,36,41,42].

2.2. Square-to-rectangular transformations

To make the computations tractable, we study the behavior of nanowires using the simplified 2D square-to-rectangular phase transformations, a representative phase transformations of the 3D cubic-to-tetragonal phase transformations, under the assumption of negligible strain contribution in the third direction. Here the square represents the austenite phase *A* and the rectangles represent the martensitic variants *M+* and *M−* (with rectangle length aligned along two perpendicular axes) as shown in Fig. 1. The deviatoric strain e_2 is used as the order parameter to characterize the austenite and martensite phases. We use the 2–4–6 polynomial free energy function \mathcal{F} developed in the earlier works (see [43–45] and references therein, as well as [15]):

$$\begin{aligned}\mathcal{F}_{\text{op}} &= \frac{a_2}{2} \left(\frac{\theta - \theta_m}{\theta_m} \right) e_2^2 - \frac{a_4}{4} e_2^4 + \frac{a_6}{6} e_2^6, \\ \mathcal{F}_{\text{nop}} &= \frac{a_1}{2} e_1^2 + \frac{a_3}{2} e_3^2, \\ \mathcal{F}_{\text{gradient}} &= \frac{k_g}{2} \left[\left(\frac{\partial e_2}{\partial x} \right)^2 + \left(\frac{\partial e_2}{\partial y} \right)^2 \right],\end{aligned}\quad (3)$$

where a_1 is the bulk modulus, a_3 is the shear modulus, a_2 , a_4 , a_6 are the Landau constants, k_g is the Ginzburg coefficient, θ is the material temperature, and θ_m is the austenite–martensite transformation temperature, which depends upon the alloy concentration and manufacturing process.

The strains for square-to-rectangular phase transformations are defined as:

$$e_1 = (\epsilon_{xx} + \epsilon_{yy})/\sqrt{2}, \quad e_2 = (\epsilon_{xx} - \epsilon_{yy})/\sqrt{2}, \quad e_3 = (\epsilon_{xy} + \epsilon_{yx})/2, \quad (4)$$

where e_1 , e_2 , e_3 are the hydrostatic, deviatoric, and shear strain respectively, the Cauchy–Lagrange strain tensor is defined as $\epsilon_{ij} = [(\partial u_i / \partial x_j) + (\partial u_j / \partial x_i)]/2$ (using the repeated index convention) with $\epsilon_{xy} = \epsilon_{yx}$, and u_i , $i = 1, 2$ are the displacements along x , and y direction, respectively. The model is developed based on an isotropic material properties within the small strain framework.

As per the Landau theory, the free energy is defined in such a way that it accounts for temperature dependency. When the temperature is higher than the phase transformation temperature θ_m , the Landau energy function has a minimum corresponding to the austenite phase. When the temperature is lower than θ_m , the energy has several minimum corresponding to the variants of martensite. When the temperature is near θ_m , the Landau free energy have minima corresponding to the austenite and the martensite variants. Fig. 2 shows the dependence of free energy on temperature in square-to-rectangular PTs.

The SMA may exhibit ferroelastic, pseudoelastic and elastic behavior at low, intermediate and high temperatures [38,46]. These wide ranges of qualitative behaviors are captured in the sim-

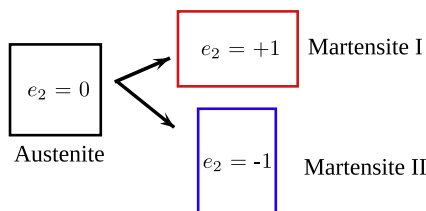


Fig. 1. Square-to-rectangular transformations (value of OP e_2 denotes different phases).

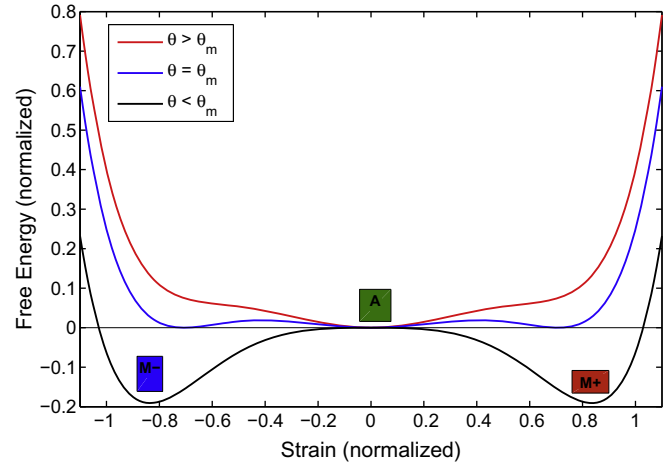


Fig. 2. Free Energy of square-to-rectangular PT as the function of temperature. The square (green color) box represents Austenite (*A*) phase, and rectangles (red and blue colors) represent Martensite variants (*M+* and *M−*).

ulations by accounting for the coupling effects between the structural and thermal field dynamics. A mathematical model that accounts for this coupling is developed based on the three fundamental laws: conservation of mass, conservation of linear momentum, and energy balance [47].

The governing equations for the mechanical, and thermal field are obtained by minimizing the total energy in the domain. The kinetic energy \mathcal{K} of the system is expressed as

$$\mathcal{K}(t) = \frac{\rho}{2} (\dot{u}_1^2 + \dot{u}_2^2), \quad (5)$$

where ρ is the mass density, and \dot{u}_1 and \dot{u}_2 are the velocities in x , and y directions, respectively.

We assume the dissipation functional \mathcal{R} as

$$\mathcal{R}(u_1, u_2, t) = \frac{\eta}{2} (\dot{u}_{1,1}^2 + \dot{u}_{1,2}^2 + \dot{u}_{2,1}^2 + \dot{u}_{2,2}^2), \quad (6)$$

where η is the dissipation coefficient, \dot{u}_{ij} refers to the velocity of u_i in j direction, with $i, j = 1, 2$ [48].

The Lagrangian \mathcal{L} of the system is defined as

$$\mathcal{L}(u_1, u_2, \theta, t) = \mathcal{K}(t) - \mathcal{F}(u_1, u_2, \theta) - \mathcal{R}(u_1, u_2, t). \quad (7)$$

Then, the Hamiltonian \mathcal{H} of the system is

$$\mathcal{H} = \int_0^t \int_{\Omega} (\mathcal{L}(u_1, u_2, \theta) - f_1 u_1 - f_2 u_2) d\Omega dt, \quad (8)$$

where f_1 and f_2 are mechanical loadings in x , and y direction, respectively, Ω is the SMA domain, and $[0, t]$ is the time span.

According to the Hamiltonian principle, the first variation of the total energy in the domain is zero, provided the displacement u_i give the solution to the structural part of the problem. The Euler–Lagrange equations associated with Eq. (8) can be obtained by solving

$$\delta u_i: \frac{\partial \mathcal{L}}{\partial u_i} - \sum \frac{\partial}{\partial x_i} \left(\frac{\partial \mathcal{L}}{\partial u_{i,i}} \right) + \sum \frac{\partial^2}{\partial x_i \partial x_j} \left(\frac{\partial \mathcal{L}}{\partial u_{i,ij}} \right) - \frac{\partial}{\partial t} \left(\frac{\partial \mathcal{L}}{\partial \dot{u}_i} \right) - \frac{\partial \mathcal{L}}{\partial \dot{u}_i} = 0, \quad (9)$$

where $u_{i,i}$ and $u_{i,ij}$ are the first and second order partial differential terms with respect to spatial variables.

On substituting Eqs. (2)–(8) in Eq. (9), we obtained the mechanical (or structural) dynamics equilibrium equations

$$\rho \frac{\partial^2 u_i}{\partial t^2} = \sum \frac{\partial \sigma_{ij}}{\partial x_j} + \sigma_{g_i} + \eta \nabla^2 \dot{u}_i + f_i, \quad (10)$$

where $\sigma_{ij} = \frac{\partial}{\partial \epsilon_{ij}} (\mathcal{F}_{\text{op}} + \mathcal{F}_{\text{nop}})$ and $\sigma_{g_i} = \frac{\partial}{\partial \epsilon_{g_i}} (\mathcal{F}_{\text{gradient}})$.

With the assumption that the deformation in the third direction is zero for 2D square-to-rectangular transformations, the stress tensor σ_{ij} components are simplified to

$$\sigma_{11} = \frac{1}{\sqrt{2}} \left[a_1 e_1 + a_2 \left(\frac{\theta - \theta_m}{\theta_m} \right) e_2^2 - a_4 e_2^3 + a_6 e_2^5 \right], \quad (11.1)$$

$$\sigma_{12} = \frac{1}{2} a_3 e_3, \quad (11.2)$$

$$\sigma_{21} = \sigma_{12}, \quad (11.3)$$

$$\sigma_{22} = \frac{1}{\sqrt{2}} \left[a_1 e_1 - a_2 \left(\frac{\theta - \theta_m}{\theta_m} \right) e_2^2 + a_4 e_2^3 - a_6 e_2^5 \right], \quad (11.4)$$

and the σ_{g_i} components to

$$\sigma_{g_1} = k_g \left[\frac{\partial^4 u_1}{\partial x_1^4} + \frac{\partial^4 u_1}{\partial x_2^2 \partial x_2^2} - \frac{\partial^4 u_2}{\partial x_1^3 \partial x_2} - \frac{\partial^4 u_2}{\partial x_1 \partial x_2^3} \right], \quad (12.1)$$

$$\sigma_{g_2} = k_g \left[-\frac{\partial^4 u_1}{\partial x_1^3 \partial x_2} - \frac{\partial^4 u_1}{\partial x_1 \partial x_2^3} + \frac{\partial^4 u_2}{\partial x_1^2 \partial x_2^2} + \frac{\partial^4 u_2}{\partial x_2^4} \right]. \quad (12.2)$$

Eq. (11) defines the material behavior in square-to-rectangular PTs. The equations for σ_{ij} are highly non-linear (quintic non-linearity allows us to capture the PT properties like shape memory effect and pseudoelasticity as a function of temperature). The 4th order differential terms in Eq. (12) represent domain walls between different phases of martensites.

The governing equation of the thermal field is obtained by the conservation law for internal energy e [47] as

$$\rho \frac{\partial e}{\partial t} - \sigma^T : \nabla \mathbf{v} + \nabla \cdot \mathbf{q} = g, \quad (13)$$

where $\mathbf{q} = -\kappa \nabla \theta$ is the Fourier heat flux vector, κ is the heat conductance coefficient of the material, and g is a thermal loading. The internal energy is connected with the potential energy constructed above via the Helmholtz free energy Ψ as

$$e = \Psi(\theta, \epsilon) - \theta \frac{\partial \Psi(\theta, \epsilon)}{\partial \theta}, \quad (14)$$

$$\Psi(\theta, \epsilon) = \mathcal{L}(u_1, u_2, \theta) - c_v \theta \ln \theta,$$

where c_v is the specific heat of a material.

On substituting the above relationship in Eq. (13), the governing equation of the thermal field is formulated as

$$\rho c_v \frac{\partial \theta}{\partial t} = \kappa \left(\frac{\partial^2 \theta}{\partial x^2} + \frac{\partial^2 \theta}{\partial y^2} \right) + a_2 \frac{\theta}{\theta_m} e_2 \frac{\partial e_2}{\partial t} + g. \quad (15)$$

The second term on the right-hand side of Eq. (15) is a non-linear term, which couples temperature, deformation gradient (strain), and rate of deformation gradient (strain rate). Hence the overall system equations (Eqs. (10) and (15)) constitute the thermo-mechanical physics by creating the two-way coupling via θ , e_2 and \dot{e}_2 .

As both the structural dynamics equations (Eq. (10)) and thermal dynamics equation (Eq. (15)) are derived from the same free energy \mathcal{F} of PT, the equations for SMA dynamics are intrinsically coupled. This approach is a direct extension of the one dimensional Falk approach analyzed numerically and discussed extensively in our earlier work [13,22,23,45]. In this paper, we have introduced the nanoscale length implicitly in the model via the Ginzburg coefficient. We do not consider the effects of plasticity and explicit incorporation of surface effects on the properties of constrained SMA nanostructures (as the constrained boundary conditions used in the simulations override the surface stresses observed in nanosize specimens [49]). The details of these effects are discussed elsewhere in the literature [1,50].

The analysis of SMA dynamics in Eqs. (10) and (15) is very involved due to strong material non-linearity and interactions between mechanical and thermal fields (see [51] for the one-dimensional analysis). In this paper, we use the finite element method as a numerical tool to study the MTs. To model the MTs at the nanoscale using the finite element method, two main challenges were observed. Firstly, the length scale in the nanometer range (10^{-9} m) causes numerical difficulties in using material properties in kg-m-s-K (SI) unit system. Secondly, the time step needed for nanoscale dimensions in SI unit system is very small (in the range of 1 ps). These challenges create numerical difficulties to simulate the highly nonlinear coupled thermo-mechanical physics. To circumvent these difficulties, the equations have been rescaled (non-dimensionalized) in the spatial and temporal domain, as described in Appendix A. The fourth order partial differential terms were expressed as two second order partial differential terms. The rescaled equations were converted into the generalized form compatible with the Comsol Multiphysics® software. The generalized forms of equations have been implemented by defining the strains, constitutive relations and equilibrium equations. The equations were solved in dimensionless form and the results were converted back to physical units. The microstructures and mechanical properties of nanowires and nanograins for 2D square-to-rectangular PTs are presented in Section 4.

In the following section, we derive a semi-analytical model to predict the onset of martensitic transformation suppression phenomenon observed experimentally [52] and numerically [15] in SMA nanoscale samples upon cooling. We base our consideration on the developed PF model for square-to-rectangular phase transformations.

3. Analytical prediction of the martensitic transformation suppression phenomenon

The MT is characterized by the formation of martensitic twin microstructure in the SMA system on cooling, below the martensitic transformation temperature. The number of martensitic twins decrease with decreasing nanograin size. The microstructure completely disappears below a certain size of the nanostructure called the MT suppression limit (which is characterized by the critical size of the nanostructure). The experiments showed the MT suppression phenomenon below 50 nm grain size in NiTi nanocrystals [24]. The MT suppression is caused by a change in the strain distribution due to the increase in surface-to-volume ratio in the constrained SMA nanosystems. We have also observed the MT suppression during the numerical simulations (described in detail in Section 4.1). It is important to predict the MT suppression size at the operating temperature for application developments. The model will also assist in predicting the MT suppression in nanosystems that is observed during their microstructure evolution.

The MT suppression is exemplified using a simple simulation of microstructure evolution in square nanograins of size 80 nm, as well as 60 nm. The material properties, initial and boundary conditions used during the microstructure evolution are given in Section 4.1. The evolved microstructures in square nanograins cooled to 250 K are shown in Fig. 3. The martensitic variants are represented in Fig. 3a by two oriented rectangles and the austenite phase by a square near the boundaries in the 80 nm nanograin. However, in Fig. 3b, the austenite (square) phase is stabilized with no nucleation of martensite, indicating the influence of constrained boundaries on the microstructure evolution in the 60 nm nanograin.

The LGD phenomenology has been used before to derive the critical size of ferroelectric systems [53,54] and nanostructures [28,55,56]. We also use the LGD phenomenology for the analytical description of the critical size. Since here we are interested in PTs

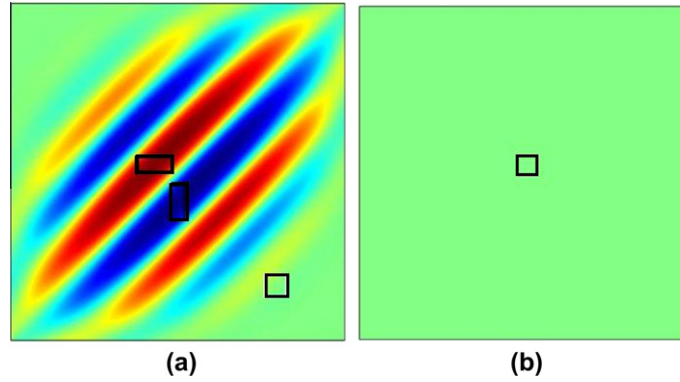


Fig. 3. Evolution of microstructure in square nanograins of size (a) 80 nm, (b) 60 nm. The square box represents austenite phase, and rectangles represent martensite variants.

and critical size, the contributions due to \mathcal{F}_{nop} are neglected in free energy Eq. (2). As the nanostructure is cooled and kept below the transformation temperature (in a temperature controlled environment), the coupled thermo-mechanical physics is reduced to purely mechanical (or structural) physics. The free energy in Eq. (2) is reduced to the free energy \mathcal{F}_{PT} of PT as

$$\mathcal{F}_{\text{PT}} = \mathcal{F}_{\text{op}} + \mathcal{F}_{\text{gradient}}. \quad (16)$$

By using Eq. (3), for square-to-rectangular transformation, the free energy of PT takes the form

$$\mathcal{F}_{\text{PT}} = \int_{\Omega} \left\{ \frac{a_2}{2} \left(\frac{\theta - \theta_m}{\theta_m} \right) e_2^2 - \frac{a_4}{4} e_2^4 + \frac{a_6}{6} e_2^6 + \frac{k_g}{2} \left[\left(\frac{\partial e_2}{\partial x} \right)^2 + \left(\frac{\partial e_2}{\partial y} \right)^2 \right] \right\} dx dy, \quad (17)$$

where, as before, e_2 is the deviatoric strain.

The critical size of SMA nanosystems is derived by defining an appropriate energy functional and determining the minimum of that functional using the calculus of variations. The model for the free energy in Eq. (17) is simplified with the following assumptions (refer to Fig. 4) for a nanostructure close to the critical size:

- there exists no twin boundaries in the nanostructure,
- the deviatoric strain e_2 distribution is symmetric along the center line in x and y directions in the square nanograin,
- the deviatoric strain e_2 is a function of distances x and y from the centerline of the square nanograin, and
- the deviatoric strain e_2 is a one dimensional function (with respect to \tilde{x} direction).

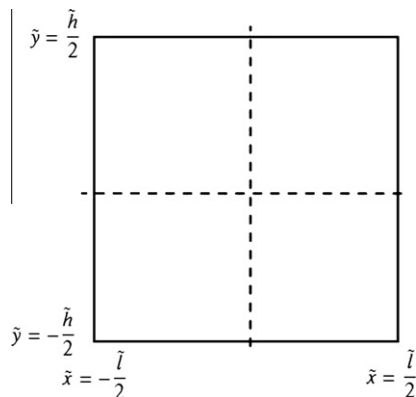


Fig. 4. Schematic of a nanograin for size effect prediction.

The free energy is rescaled (non-dimensionalized) in the spatial dimension as described in Appendix B. Assuming $\tilde{e}_2 = \tilde{e}$, we define the functional $\tilde{I}(\tilde{e})$ in the interval $(-\tilde{l}/2, \tilde{l}/2)$ as

$$\tilde{I}(\tilde{e}) = \int_{\tilde{\Omega}} \tilde{\mathcal{F}}_{\text{PT}}(\tilde{x}, \tilde{e}, \tilde{e}_{,\tilde{x}}) d\tilde{x} = \int_{\tilde{\Omega}} \left\{ \frac{1}{2} \tilde{a}_2 \tilde{e}^2 - \frac{1}{4} \tilde{e}^4 + \frac{1}{6} \tilde{e}^6 + \frac{1}{2} \left(\frac{d\tilde{e}}{d\tilde{x}} \right)^2 \right\} d\tilde{x}. \quad (18)$$

The functional $\tilde{I}(\tilde{e})$ represents the free energy of phase transformations as a continuous function of space \tilde{x} , strain \tilde{e} , and its derivative. The solution to the $\tilde{I}(\tilde{e})$ leads to an extremum of the functional. The minimum of the functional $\tilde{I}(\tilde{e})$ can be determined by using the Euler-Lagrange equation as in [57]

$$\frac{d\tilde{\mathcal{F}}_{\text{PT}}}{d\tilde{e}} - \frac{d}{d\tilde{x}} \left(\frac{d\tilde{\mathcal{F}}_{\text{PT}}}{d\tilde{e}_{,\tilde{x}}} \right) = 0. \quad (19)$$

On solving Eq. (19), we obtain

$$\frac{d^2 \tilde{e}}{d\tilde{x}^2} = \tilde{a}_2 \tilde{e} - \tilde{e}^3 + \tilde{e}^5. \quad (20)$$

For $\theta < \theta_m$, Eq. (20) has five roots: a trivial root $\tilde{e} = 0$, two symmetric imaginary roots, and two symmetric real roots. The size effects in ferroelectric particles are obtained by incorporating slope boundary condition as a function of extrapolation length [54]. In the absence of experimental values of extrapolation length for FePd nanoparticles, we apply the following boundary conditions:

$$\left. \frac{d\tilde{e}}{d\tilde{x}} \right|_{\tilde{x}=0} = 0, \quad \tilde{e}|_{\tilde{x}=\tilde{l}/2} = \frac{\tilde{l}}{2} = 0.8\tilde{e}. \quad (21)$$

As the distribution of the deviatoric strain \tilde{e} is symmetric, Eq. (20) is solved for only half width of the nanograin with zero strain gradient at the center ($\tilde{x} = 0$) of nanograin. The strains are non-zero at the boundaries because of the constrained boundary conditions $u_i = 0$. We carried out the simulations for different values of strains at the boundary. Here we present the results for strain at the boundary ($\tilde{x} = \tilde{l}/2$) to be equal to 0.8 times the strain at center ($\tilde{x} = 0$) of a constrained nanograin [54].

Eq. (20) is solved numerically using Maple™ software with the boundary conditions in Eq. (21). The \tilde{e}_{max} is the bulk strain that represent the positive real root of the right-hand side of Eq. (20). In the constrained nanograin, the deviatoric strain \tilde{e} is equal to \tilde{e}_{max} at the centre. The deviatoric strain distribution is uniform within a domain and varies near a boundary. We consider the deviation of strain \tilde{e} from \tilde{e}_{max} at the centre and variation of strain in the whole domain as an onset of MT suppression phenomenon. We have studied the spatial distribution of deviatoric strain and effect of temperature on nanograins of different sizes.

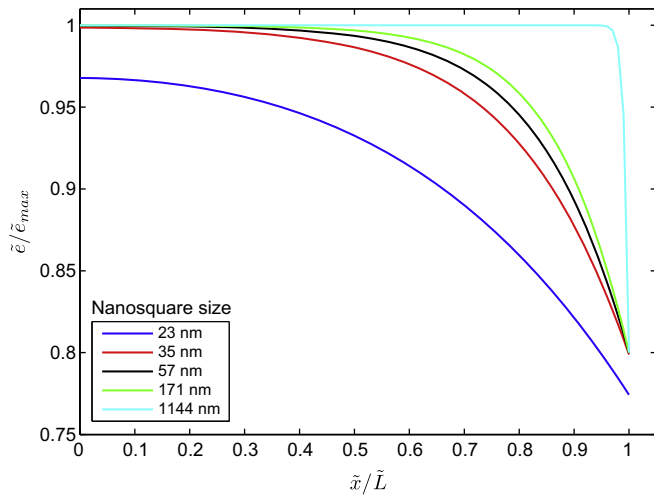


Fig. 5. Deviatoric strain $\bar{\epsilon}/\bar{\epsilon}_{max}$ distribution (normalized) in the half width of the nanograin \bar{x}/\bar{L} (normalized distance) at temperature 250 K.

Fig. 5 shows the normalized deviatoric strain distribution ($\bar{\epsilon}/\bar{\epsilon}_{max}$) in nanograins of varying sizes (\bar{x}/\bar{L}) at temperature 250 K ($\bar{L} = \bar{l}$). It is apparent that the deviatoric strain distribution in larger nanograins (> 171 nm) is uniform within a domain and varies drastically near the boundary at $\bar{x} = \bar{l}/2$. As the nanograin size decreases, the variation of strain is observed throughout the nanograin. It is observed that the value of $\bar{\epsilon}$ starts deviating from value of $\bar{\epsilon}_{max}$ around 57 nm. At nanograin size smaller than 57 nm, there are drastic variations in the deviatoric strain distribution. The variation of strain in smaller nanograins indicates the increased influence of boundaries. The critical size obtained at temperature 250 K is around 57 nm in this case, which is in close agreement with the numerical simulation results (60 nm) during microstructure evolution.

The numerical experiments were carried out for nanograins of different sizes at a fixed temperature to obtain the critical size. The experiments were repeated to obtain critical sizes at different temperatures. Fig. 6 shows the effect of temperature on the critical size in a square nanograin. It is apparent that the decrease in temperature inhibits the MT in nanograins of smaller sizes. Hence, the reduction in temperature and size is favorable for the MT suppression.

In summary, we have developed a semi-analytical model to predict the onset of MT suppression phenomena based on the

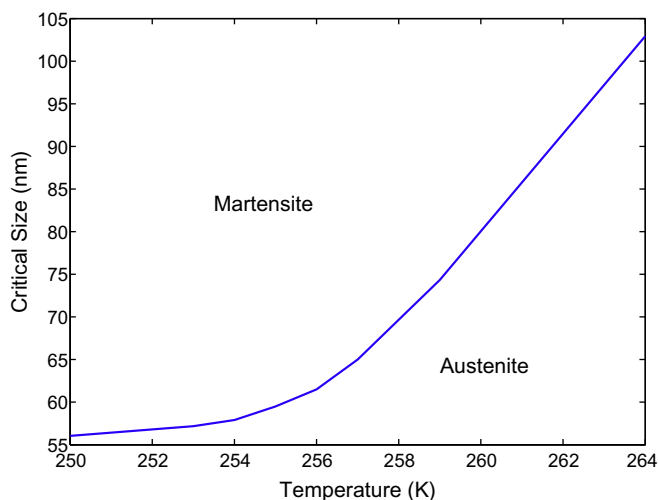


Fig. 6. Critical size dependence on temperature in square nanograin.

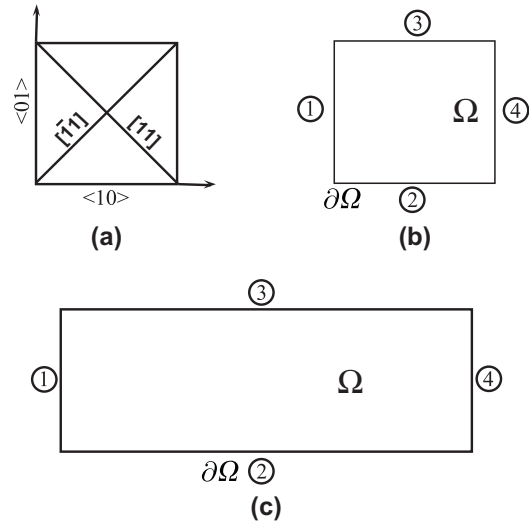


Fig. 7. Schematic indicating (a) direction and plane in the parent crystal (b) square nanograin and (c) nanowire boundary ($\partial\Omega$) nomenclature in the domain (Ω).

Ginzburg–Landau energy. The deviation of deviatoric strain (at the centre of nanograin) from the bulk value and variation of deviatoric strain in the whole domain is considered as an onset of MT suppression. The predicted critical size is in good agreement with the numerical results. The model can be improved by incorporating boundary conditions based on extrapolation length obtained from the experiments. The modeling methodology can be extended to other PTs for quick prediction of critical sizes.

4. Numerical simulations of SMA nanostructures

In this section, we provide the details of the numerical experiments on SMA nanowires and nanograins to study the effect of thermo-mechanical coupling on microstructures and mechanical properties. The SMA dynamics is modeled by solving the coupled thermo-mechanical model developed for square-to-rectangular transformations in Section 2.2. The governing equations are 4th order partial differential equations in space. Numerical methodologies like finite difference [14,32,58], finite volume [45], or spectral methods [7,11,59] have been traditionally used for higher order equations. These methodologies are usually limited to simple geometries. The finite element method (FEM) allows us to simulate wide varieties of loadings and boundary conditions on complex geometries. In the context of SMA, the FEM was initially applied to the analysis of one dimension phase transformation dynamics (e.g. [60,61]). More recently the FEM has been used by other groups [16,62,63] for 2D and 3D simulations. In what follows, all numerical experiments have been carried out by using the finite element methodology. The mechanical and thermal field equations have been solved simultaneously. It is well known that the strong inherent non-linearities and coupling between mechanical and thermal fields present non-trivial difficulties in the solution of the corresponding equations [45,47].

In the following subsections, we first study the microstructure evolution subjected to constrained boundaries and then perform the tensile test to study mechanical properties of these evolved microstructures.

4.1. Microstructures

The microstructures were evolved in nanowires and nanograins of different sizes. In general, a cylindrical nanowire is reduced to two dimensional rectangular geometry (e.g. [15]). A nanostructure

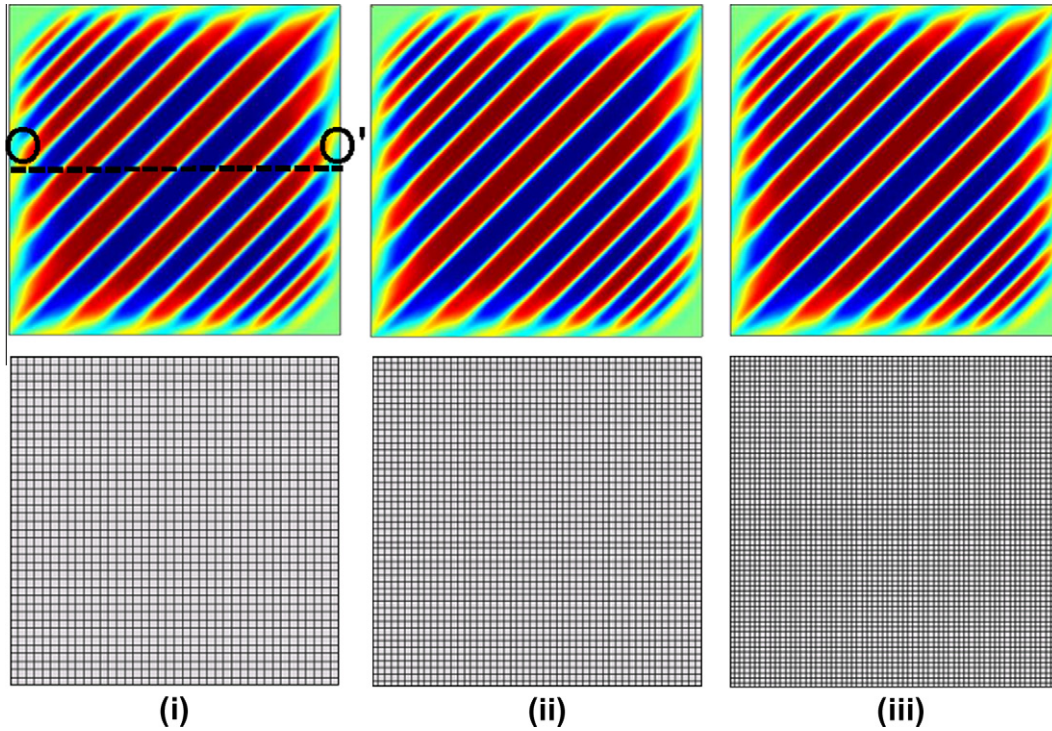


Fig. 8. Mesh sensitivity study on square nanograin of size 200 nm. The top row represent the deviatoric strain distribution for different meshes in the bottom row. The meshes used for simulations are (i) 1600 elements (73 k DOF), (ii) 2500 elements (114 k DOF), and (iii) 4225 elements (192 k DOF).

in the austenite phase ($\theta > \theta_m$) was allowed to evolve into the martensitic microstructures below the transformation temperature ($\theta < \theta_m$). The simulations were conducted for nanowires of 2000 nm in length and varying widths, as well as for square nanograins of varying sizes from 200 nm to 50 nm. The nanostructure domains were modeled with sides parallel to [01] and [10] directions of the parent austenite phase as shown in Fig. 7. The nanostructures were mechanically constrained and thermally insulated on all the boundaries (1–4) during the microstructure evolution. The microstructure has been evolved by allowing the nanostructures in the austenite phase $\theta > \theta_m$ (265 K) to evolve by quenching to temperature $\theta = 250$ K with the following boundary and initial conditions:

$$\begin{aligned} u_i|_{(\partial\Omega=1-4,t)} &= 0, \quad \theta|_{(\Omega,t=0)} = \theta_{\text{init}}, \quad \nabla u_i \cdot \mathbf{n}|_{(\partial\Omega=1-4,t)} = 0, \\ \nabla \theta \cdot \mathbf{n}|_{(\partial\Omega=1-4,t)} &= 0, \\ u_1|_{(\Omega,t=0)} &= x(l-x)y(h-y) \times 10^{-8}, \quad u_2|_{(\Omega,t=0)} = 0, \end{aligned} \quad (22)$$

where l and h are the length and width of a nanosystem, and \mathbf{n} is the normal vector to the boundary.

The simulations were performed for homogeneous single crystal FePd material with the following material parameters found in [15,64]:

$$\begin{aligned} a_1 &= 140 \text{ GPa}, \quad a_3 = 280 \text{ GPa}, \quad a_2 = 212 \text{ GPa}, \quad a_4 = 17 \times 10^3 \text{ GPa}, \\ a_6 &= 30 \times 10^6 \text{ GPa}, \quad \theta_{\text{init}} = 250 \text{ K}, \quad \theta_m = 265 \text{ K}, \\ c_v &= 350 \text{ J kg}^{-1} \text{ K}^{-1}, \quad \kappa = 78 \text{ W m}^{-1} \text{ K}^{-1}, \quad \text{and } \rho = 10,000 \text{ kg m}^{-3}. \end{aligned}$$

The spatial and temporal domains have been rescaled (non-dimensionalized) by constants 1.808×10^{-9} m, and 1.842×10^{-12} s, respectively (see Appendix A).

The mesh sensitivity of the numerical solution was investigated on a square nanograin of size 200 nm by evolving the microstructures with different finite element meshes. Fig. 8 shows the distribution of evolved deviatoric strain e_2 for three different meshes:

(i) 1600 elements (73 k degrees of freedom (DOF)), (ii) 2500 elements (114 k DOF), and (iii) 4225 elements (192 k DOF). The microstructure distribution is identical for all meshes. The error has been evaluated for deviatoric strain e_2 along the cut-line $O - O'$ for mesh (i) and (ii) w.r.t. the mesh (iii) and plotted in Fig. 9. The errors due to the discrete mesh (i) and (ii) are very small (less than 2×10^{-3}), indicating that the numerical results are practically mesh independent.

The numerical simulations were performed on the Linux workstation with Intel Xeon 2.0 GHz CPU, eight processors, and 32 GB RAM. We have used cubic Lagrangian elements to mesh the domain. The stabilized microstructures were observed in approximately 2 h with the finest mesh (mesh (iii)). The simulation was completed in 3.5 h for 5000 time units (equivalent to 9.2 ns). The memory usage of 4 GB was required with the finest mesh. The relative error criterion of 1×10^{-6} has been used for numerical convergence. The simulations were performed with an adaptive time stepping. The evolution of timestep for mesh (iii) is shown in Fig. 10. It took more than 6000 total time steps for complete simulation. Initially, the nonlinear solver took smaller time steps during the microstructure formation, but eventually it took larger timesteps upon microstructure stabilization.

4.1.1. Thermal effects in nanowire microstructures

The martensitic microstructures were evolved in the constrained nanowires of different sizes by quenching them to temperature 250 K. The microstructures were allowed to evolve, by minimizing the total free energy, till they were stabilized. Fig. 11 shows the plot of time evolution of rescaled free energy. The energy (and hence microstructure) has been stabilized after approximately 500 time units.

We also observed the effect of geometrical constraint on microstructures in finite size nanowires similar as it was done with an isothermal model [15]. Fig. 12 shows the evolved microstructure

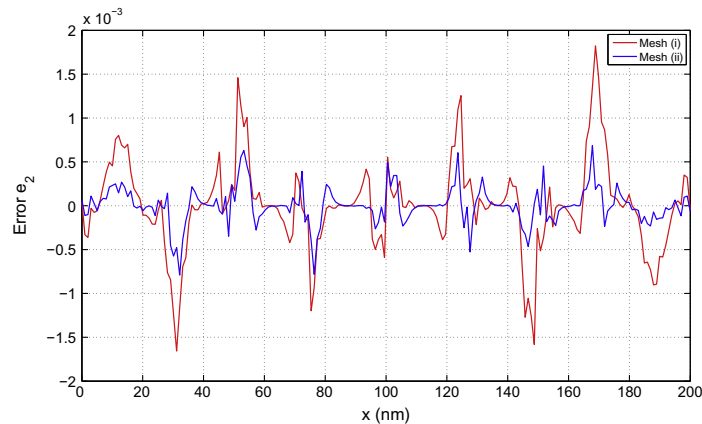


Fig. 9. Error plots for the deviatoric strain e_2 for mesh (i) and (ii) along line $O - O'$ (in Fig. 8i) w.r.t. mesh (iii).

of the nanowires of length 2000 nm and varying widths. The martensitic variants are shown in red¹ and blue color and austenite is in green color. The twin martensitic microstructures have been observed in nanowires of larger widths with a few twin switchings from $[11]$ to $[\bar{1}1]$ direction and vice versa. The twin switching increases in smaller widths nanowires. At 58 nm width, the size effect starts to dominate and complete twins running in $[11]$ to $[\bar{1}1]$ directions can no longer be formed, thus evolving to a new dot type microstructure. The size effect dominates at 55 nm, where the martensitic transformation is completely suppressed and the austenite remains untransformed. The onset of suppression of the MT is characterized by the critical width (or size) known also as the MT suppression width. Below the critical width, the confined geometry does not permit the nucleation of martensite.

During the microstructure formation, the OP e_2 evolves. The coupling of e_2 and \dot{e}_2 causes the temperature to evolve as per Eq. (15) (second term on the right-hand side). Fig. 13 shows the plot of average evolved temperature vs. nanowire width. At larger widths, the temperature is high due to larger nanowire areas. The evolved temperature decreases with the decrease in width due to the formation of fewer twins. As the martensitic microstructure does not evolve below the critical size ($e_2 = 0$ with austenite phase), the temperature evolution does not occur. An important observation made is that the temperature does not change at and below the critical size. These observations have not been captured by previous models reported in the literature [15,14].

4.1.2. Thermal effects in square nanograin microstructures

Similar microstructure evolution studies were performed on square nanograins. Fig. 14 shows the plot of time evolution of rescaled free energy. The energy (and hence microstructure) has been stabilized after approximately 500 time steps. The evolved microstructures in nanograins of different sizes are shown in Fig. 15. The twins have been observed in larger size nanograins. The dotted microstructure has been observed in the intermediate size range and the MT suppression at the critical size of 60 nm. Due to the symmetric shape and confined geometry, the twin planes are oriented in the $[\bar{1}1]$ direction and there is no switching of twin planes, as observed in the microstructures in the nanowires.

The deviatoric strain e_2 changes with the microstructure for different sizes of nanograins. Fig. 16 shows the change in maximum absolute deviatoric strain, $\max |e_2|$, for different sizes of nanograin. The $\max |e_2|$ decreases with the decrease in the nanograin size and

its value becomes zero below the critical width. The change in $\max |e_2|$ also serves as an indicator of the critical size in nanograins.

4.2. Mechanical properties of nanowires under dynamic loading conditions

For the development of SMA devices based on nanostructures, it is important to study the mechanical properties of different microstructures reported in Section 4.1 under dynamic loading conditions. The stress-strain properties of the nanowire accounting for the coupled thermo-mechanical physics have been compared with the uncoupled structural physics from the model in the literature [15]. Then, the stress-strain property of nanowires have been studied for different strain rates.

4.2.1. Mechanical behavior of nanowires with coupled and uncoupled physics

The nanowire of size 200×1000 nm has been evolved for sufficient time till the microstructure reaches its steady state. The stress-strain properties were obtained by performing the tensile test on the nanowire. The tensile tests were performed numerically on the nanowire specimens by applying the stress free boundary conditions on the boundaries 2 and 3, and ramp displacements equivalent to the uniform strain rate on the boundaries 1 and 4 out-of-material normal during loading and unloading. The adiabatic boundary conditions were applied in the thermal physics. The tensile tests have been performed on a nanowire for the coupled thermo-mechanical and uncoupled mechanical physics. We study the mechanical behavior by applying 3% axial strain in 1 ns (equivalent to 3×10^7 /s strain rate). The high strain rate is a consequence of model rescaling.

The average axial stress-strain curves of the FePd nanowire accounting for the coupled physics are shown in Fig. 17 and the microstructures at the selected points are shown in Fig. 19. The wire has been elastically loaded till point *a*. In this part, the twins extend to the surface and the strains are accommodated elastically. A decrease in stress has been observed at the onset of detwinning transformation (unfavored martensite (blue color) converted to favored one (red color)) at the ends of the nanowire. This region *a*–*b* is marked by the sudden disappearance of martensitic twins. The wire again starts loading elastically till point *c* after the disappearance of martensitic twins. In the region *c*–*d*, the strain increases significantly with small increase in stress. The martensitic twins disappear due to the detwinning of the unfavored martensite variant to the favored martensite variant during loading. Almost all of the martensitic twins disappear and only the favored martensite variant remains at point *d*. Beyond the point *d*, the favored

¹ For interpretation of color in Figs. 2,3,5,8,9,12,15,17–22, the reader is referred to the web version of this article.

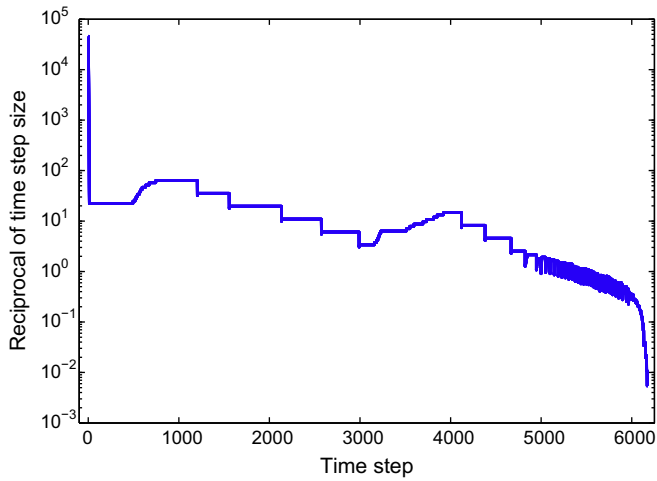


Fig. 10. Evolution of an adaptive timestep for mesh (iii).

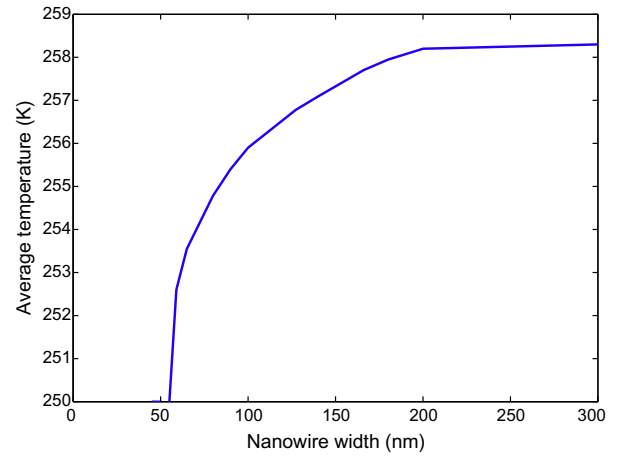


Fig. 13. Evolved temperature of FePd nanowire of constant length 2000 nm and varying width (initial temperature 250 K).

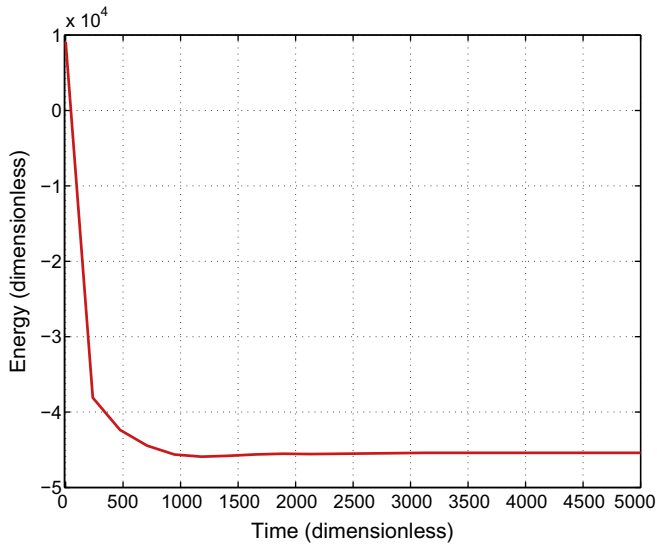


Fig. 11. Evolution of energy in the nanowire of dimension 2000×200 nm.

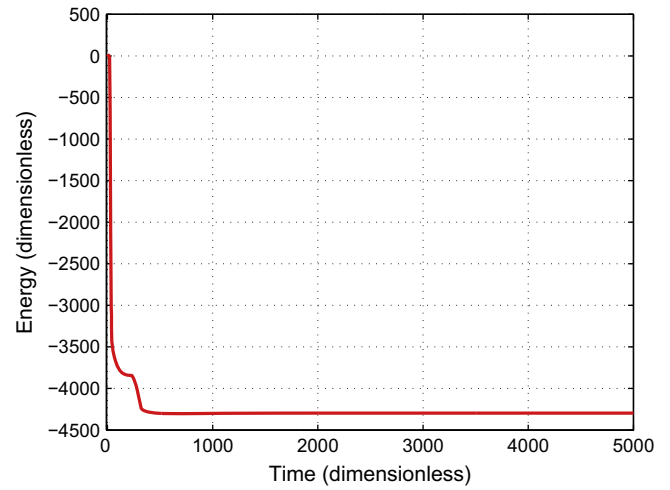


Fig. 14. Evolution of energy in the square nanograin of size 200 nm.

martensite variant is loaded elastically. If the nanowire is unloaded at point *e*, the stress–strain curve follows the path *e–f*. The microstructure at point *f* is different from the one at point *o*. The negative stress is observed at point *f* because of compressive stress generated due to the stress free boundary conditions.

The stress–strain curve has also been plotted for the nanowire accounting for the uncoupled mechanical physics in Fig. 17. The initial elastic loading till point *a* is the same for both coupled thermo-mechanical physics and uncoupled mechanical physics. A significant difference is observed in the stress–strain curves of the coupled and uncoupled physics during detwinning phase transformations in this case. The stress–strain curve of the coupled thermo-mechanical physics is qualitatively similar, but have a

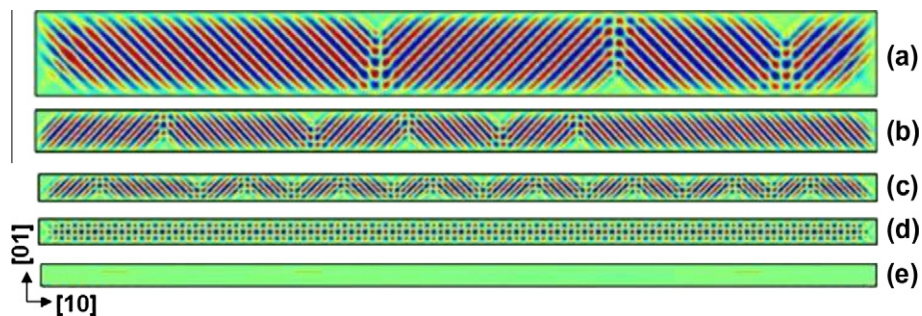


Fig. 12. Evolution of microstructure in nanowires considering coupled thermo-mechanical physics for length 2000 nm and width (a) 200 nm (b) 90 nm (c) 62 nm (d) 58 nm and (e) 50 nm (red and blue indicate martensite variants and green indicates austenite phase).

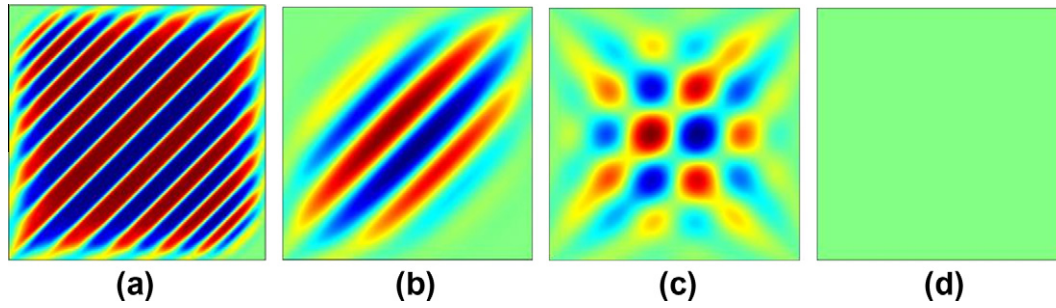


Fig. 15. Evolution of microstructure in square nanograins of size (a) 200 nm (b) 70 nm (c) 65 nm (d) 60 nm (red and blue indicate martensite variants and green indicates austenite phase).

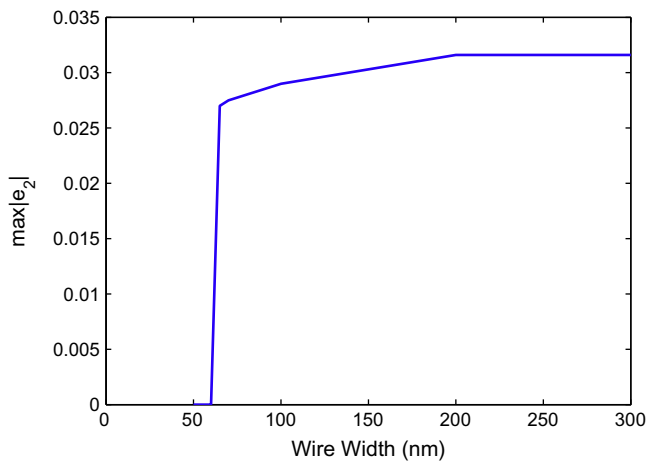


Fig. 16. Deviatoric strain $\max|e_2|$ as a function of size of square nanograin.

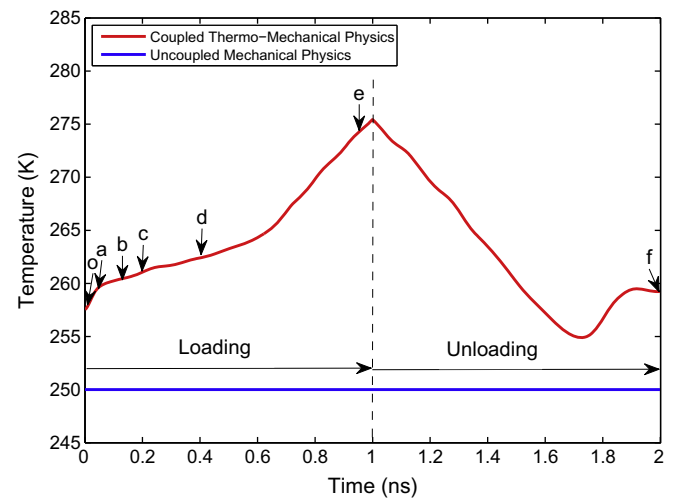


Fig. 18. Comparison of evolved temperature, during loading (0–1 ns) and unloading (1–2 ns) of nanowire for coupled and uncoupled physics with strain rate $3 \times 10^7/s$. The marker points corresponds to the points indicated in Fig. 17.

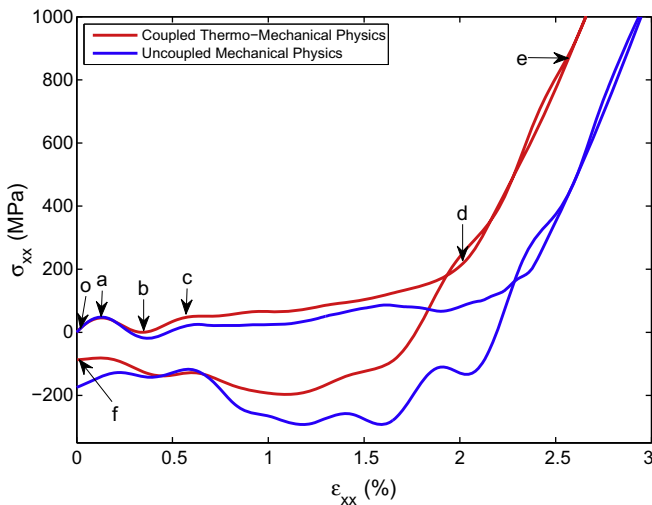


Fig. 17. Comparison of stress-strain curve of 200×1000 nm nanowires, during loading and unloading for coupled thermo-mechanical and uncoupled mechanical physics with strain rate $3 \times 10^7/s$.

steeper slope than the uncoupled mechanical physics. The shift in stress-strain curve is caused due to the increase and decrease in temperature during loading and unloading, respectively, as shown in Fig. 18. During the axial loading in x -direction, $\dot{e}_2 > 0$ (since $\dot{u} > 0$), the temperature increases due to coupling between e_2 , \dot{e}_2 , and θ in Eqs. (10) and (15). During unloading $\dot{e}_2 < 0$ (since $\dot{u} < 0$) and the coupling causes decrease in temperature. The two-way

coupling between thermal and mechanical fields, inherent to SMA, is captured by the model. On the other hand, there is no change in temperature in the uncoupled case as the loading and unloading process is isothermal. Pieczyska et al. [18,19] experimentally observed a similar behavior of temperature increase and decrease during loading and unloading of SMA specimens.

The detwinning of martensite is completed at 1.9% strain in the coupled thermo-mechanical physics and at 2.3% strain in the uncoupled mechanical physics during the loading stage. The early completion of detwinning in coupled mechanical physics is due to the increase in temperature, which aids the motion of twins during loading. During unloading, the transformation starts at 1.6% strain in the case of coupled thermo-mechanical physics and at 2.1% in the uncoupled mechanical physics. The temperature dependent stress-strain behavior in nanostructures cannot be captured with the uncoupled physics model.

4.3. Tensile test study on nanowires of different sizes

The tensile tests have been performed numerically on the nanowires of different sizes at a constant strain rate $3 \times 10^7/s$. Fig. 20 shows the stress-strain curves of nanowires of different sizes during loading. It is observed that the stress-strain curves in nanowires are weakly dependent on widths less than 200 nm, contrary to the expectation that different microstructures produce different stress-strain curves. The insignificant difference in stress-strain loading curves in smaller width nanowires is due to strain accommodation during the phase transformation. The

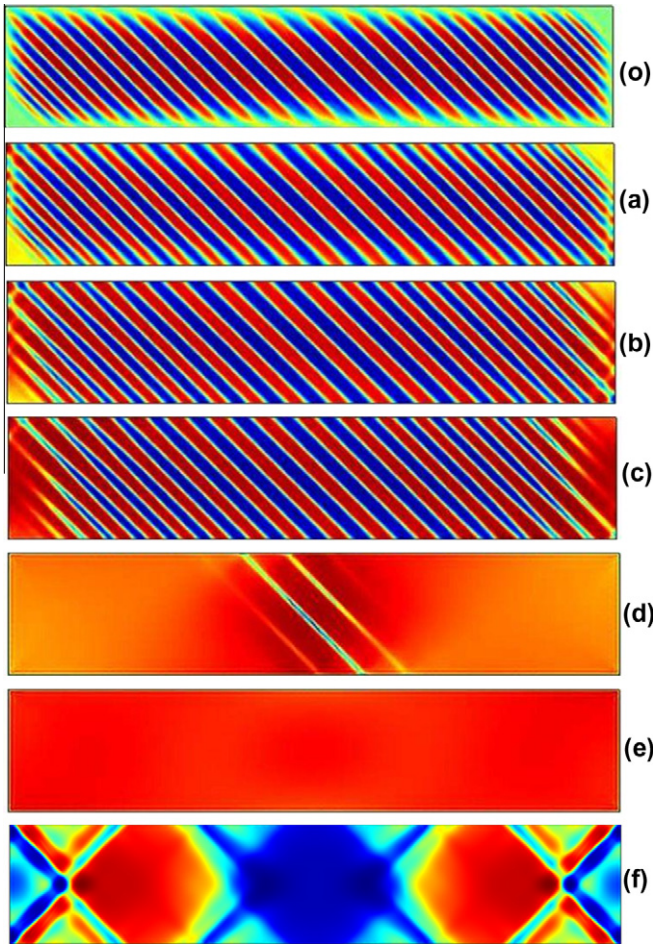


Fig. 19. Microstructures of nanowires during loading at the marker points indicated in Fig. 17 (red and blue indicate martensite variants and green indicates austenite).

strains are accommodated at nearly constant stress until all the unfavorable martensitic variants are completely transformed to the favorable variants, which is marked distinctly by a change in the stress–strain slope. The transformed favored martensitic variant starts loading elastically again.

On the other hand, for the nanowires of larger widths (widths greater than 200 nm), the stress–strain behaviors are different than for smaller width nanowires. The relatively larger widths nanowires have distinct loading curves. The microstructure studies during the tensile test have indicated that strains are accommodated through phase transformations and elastically loading simultaneously. Qualitatively similar behaviors were obtained experimentally, for the temperature uncontrolled case, by Pieczyska et al. [18,19] and numerically, for uncoupled physics, by Bouville and Ahluwalia [15].

4.4. Tensile tests at different strain rates

The tensile tests were conducted on the nanowire of size 200×1000 nm at different loading rates. Fig. 21 presents the stress–strain response of the nanowire to the three different strain rates: 3×10^7 /s, 5×10^7 /s, and 7.5×10^7 /s corresponding to application of 3%, 5%, and 7.5% strain in 1 ns. It is apparent that higher strain rates produce higher loading stresses due to the quicker increase in temperature as shown in Fig. 22. At lower strain rate of 3×10^7 /s, the detwinning phase transformation is completed at a nearly constant stress with the distinct point of completion, where the slope of stress–strain curve changes drastically. At higher strain

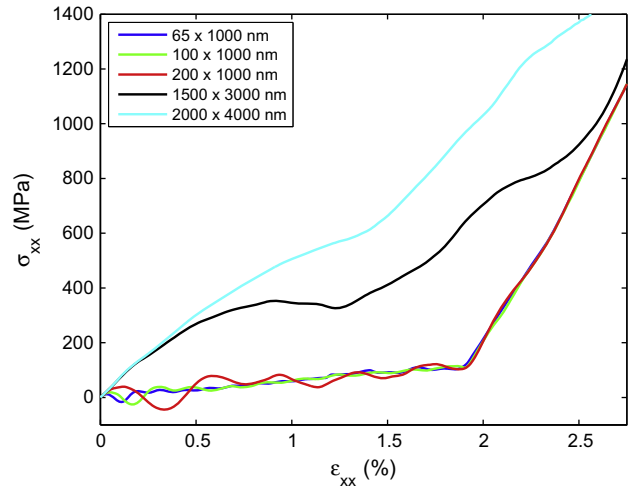


Fig. 20. Stress–strain curves of FePd nanowires of different sizes with strain rate 3×10^7 /s during loading.

rates of 5×10^7 /s, and 7.5×10^7 /s, the PT starts at higher stress and the detwinning PT does not take place at nearly constant stress due to the sudden increase in temperature, as in the case of low strain rates. The observed increase in loading stresses at higher strain rates can be attributed to the simultaneous coupled effect of structural and thermal dynamics, loading rate and the time scale of twin interface motion during the detwinning phase transformation. The higher strain rates do not give twin boundaries a time to move and complete the detwinning phase transformation at the constant stress. Instead, the detwinning phase transformation occurs along with elastic loading simultaneously, raising the stresses.

5. Discussions and conclusions

We have developed the phase field model for square-to-rectangular phase transformations in finite size constrained SMA nanostructures. The inherent thermo-mechanical properties in SMAs have been captured by coupling the structural and thermal physics. The two-way coupling has been introduced via temperature, deformation gradient (strain) and rate of deformation gradient (strain rate). We have observed a significant impact of temperature dynamics on mechanical properties, which is not captured by the models with isothermal phase transformations.

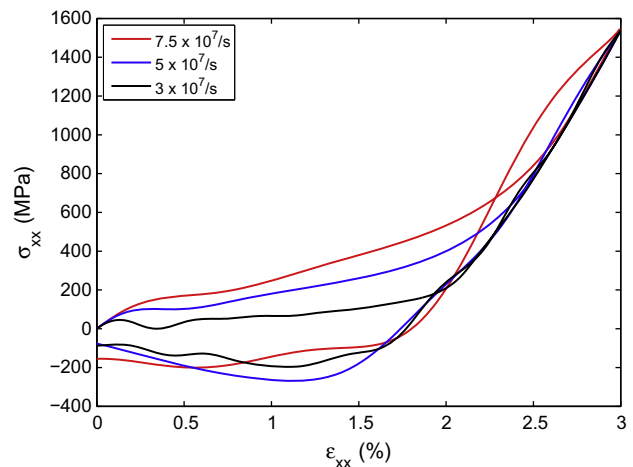


Fig. 21. Stress–strain curves of FePd nanowires of 200×1000 nm length during loading and unloading for three different strain rates: 3×10^7 /s, 5×10^7 /s, and 7.5×10^7 /s.

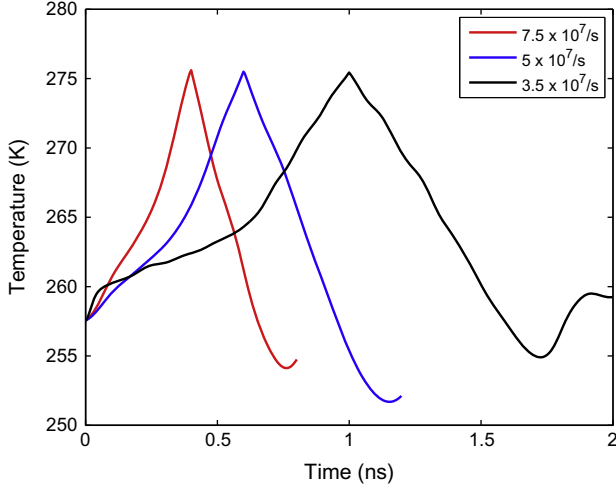


Fig. 22. Temperature evolution in FePd nanowires of 200×1000 nm length during loading and unloading for three different strain rates: $3 \times 10^7/s$, $5 \times 10^7/s$, and $7.5 \times 10^7/s$.

The microstructure evolution study showed the twin microstructures in larger size nanostructures, dotted microstructures at the intermediate size and the martensitic suppression below the critical size. The temperature increase was observed during the microstructure evolution due to creation and motion of the martensitic variants. The temperature decreases with decrease in nanostructure size, with no evolution of temperature below the critical size. We found that the temperature and maximum absolute deviatoric strain $\max|e_2|$ can serve as indicators in the study of the onset of the MT suppression.

The tensile test on the evolved nanowires showed a significant impact of thermo-mechanical coupling on the mechanical properties. The thermal physics causes the temperature to increase and decrease during loading and unloading respectively due to coupling of e_2 , \tilde{e}_2 and θ . The temperature change causes steeper slopes of stress-strain curves during the phase transformation in the coupled thermo-mechanical physics compared to the case of uncoupled mechanical physics. The temperature change also aids the motion of twins during the detwinning, causing the phase transformation to be completed early in the coupled thermo-mechanical physics.

We observed the martensitic suppression phenomenon below the critical size of nanostructures. The semi-analytical model, based on the Ginzburg–Landau theory, was developed to predict the onset of the martensitic suppression. The critical size predicted with the semi-analytical model is in good agreement with the numerical simulation results for the microstructure evolution in the case of FePd nanograins.

This study demonstrated a key importance of thermal physics in the study of properties of SMA nanostructures. We expect that the thermo-mechanical coupling will play a significant role in determining the realistic stress-strain curves in 3D PTs. In the future work, we plan to extend the developed coupled thermo-mechanical model to 3D transformations and different materials for the application of SMA nanostructures in NEMS and MEMS devices. We anticipate computational challenges in 3D simulations, however using parallel programming and rich basis function (like NURBS [65]) would make it practical.

Acknowledgments

The authors were supported by NSERC and CRC program, Canada.

Appendix A

We rescale the equations (Eqs. (3)–(15)) to a dimensionless form by using the following change of variables:

$$e_i = e_c \tilde{e}_i, \quad u_i = e_c \delta \tilde{u}_i, \quad x = \delta \tilde{x}, \quad \mathcal{F} = \mathcal{F}_c \tilde{\mathcal{F}}, \quad t = t_c \tilde{t}, \quad \theta = \theta_c \tilde{\theta}. \quad (\text{A.1})$$

The variables with tilde \sim and subscript c are rescaled variables and constants respectively. On introducing the above equations in the free energy, we obtain the rescaled free energy as:

$$\begin{aligned} \tilde{\mathcal{F}} = & \frac{1}{2} \tilde{a}_1 \tilde{e}_1^2 + \frac{1}{2} \tilde{a}_3 \tilde{e}_3^2 + \frac{1}{2} \tilde{a}_2 \tilde{e}_2^2 - \frac{1}{4} \tilde{e}_2^4 + \frac{1}{6} \tilde{e}_2^6 \\ & + \frac{1}{2} \left[\left(\frac{\partial \tilde{e}_2}{\partial \tilde{x}} \right)^2 + \left(\frac{\partial \tilde{e}_2}{\partial \tilde{y}} \right)^2 \right], \end{aligned} \quad (\text{A.2})$$

with

$$\begin{aligned} e_c = & \sqrt{\frac{a_4}{a_6}}, \quad \delta = \sqrt{\frac{k_g a_6}{a_4^2}}, \quad \tilde{a}_1 = \frac{a_1}{a_6 e_c^4}, \quad \tilde{a}_3 = \frac{a_3}{a_6 e_c^4}, \\ \tilde{a}_2 = & \frac{a_2 a_6}{a_4^2} \frac{(\theta - \theta_m)}{\theta_m}, \quad \mathcal{F}_c = \delta^2 e_c^6 a_6. \end{aligned} \quad (\text{A.3})$$

The mechanical field equations (Eq. (10)) and thermal field (Eq. (15)) can now be converted to the dimensionless form as:

$$\frac{\partial^2 \tilde{u}_i}{\partial \tilde{t}^2} = \frac{\partial \tilde{\sigma}_{ij}}{\partial \tilde{x}_j} + \tilde{f}_i, \quad (\text{A.4})$$

$$\frac{\partial \tilde{\theta}}{\partial \tilde{t}} = \tilde{k} \left(\frac{\partial^2 \tilde{\theta}}{\partial \tilde{x}^2} + \frac{\partial^2 \tilde{\theta}}{\partial \tilde{y}^2} \right) + \tilde{\chi} \tilde{\theta} \tilde{e}_2 \frac{\partial \tilde{e}_2}{\partial \tilde{t}} + \tilde{g}, \quad (\text{A.5})$$

with

$$\begin{aligned} t_c = & \sqrt{\frac{\rho \delta^2}{a_6 e_c^4}}, \quad \tilde{k} = \frac{k t_c}{\delta^2 \rho c_v}, \quad \tilde{\chi} = \frac{a_2 e_c^2}{\sqrt{2} \rho c_v \theta_c}, \quad \tilde{g} = \frac{g t_c}{\rho c_v \theta_c}, \\ \tilde{f}_i = & \frac{f_i t_c}{\rho e_c \delta}, \end{aligned} \quad (\text{A.6})$$

and the scaled components

$$\tilde{\sigma}_{11} = \frac{1}{\sqrt{2}} [\tilde{a}_1 \tilde{e}_1 + \tilde{a}_2 \tilde{e}_2 - \tilde{e}_2^3 + \tilde{e}_2^5], \quad (\text{A.7.1})$$

$$\tilde{\sigma}_{12} = \frac{1}{2} \tilde{a}_3 \tilde{e}_3, \quad (\text{A.7.2})$$

$$\tilde{\sigma}_{21} = \tilde{\sigma}_{12}, \quad (\text{A.7.3})$$

$$\tilde{\sigma}_{22} = \frac{1}{\sqrt{2}} [\tilde{a}_1 \tilde{e}_1 - \tilde{a}_2 \tilde{e}_2 + \tilde{e}_2^3 - \tilde{e}_2^5], \quad (\text{A.7.4})$$

$$\tilde{\sigma}_{g1} = \left[\frac{\partial^4 \tilde{u}_1}{\partial \tilde{x}_1^4} + \frac{\partial^4 \tilde{u}_1}{\partial \tilde{x}_1^2 \partial \tilde{x}_2^2} - \frac{\partial^4 \tilde{u}_2}{\partial \tilde{x}_1^3 \partial \tilde{x}_2} - \frac{\partial^4 \tilde{u}_2}{\partial \tilde{x}_1 \partial \tilde{x}_2^3} \right], \quad (\text{A.7.5})$$

$$\tilde{\sigma}_{g2} = \left[-\frac{\partial^4 \tilde{u}_1}{\partial \tilde{x}_1^3 \partial \tilde{x}_2} - \frac{\partial^4 \tilde{u}_1}{\partial \tilde{x}_1 \partial \tilde{x}_2^3} + \frac{\partial^4 \tilde{u}_2}{\partial \tilde{x}_1^2 \partial \tilde{x}_2^2} + \frac{\partial^4 \tilde{u}_2}{\partial \tilde{x}_2^4} \right]. \quad (\text{A.7.6})$$

The FePd material parameters used during the simulations are given in Section 4.1.

Appendix B

We rescale equation (Eq. (17)) by using the method described in Appendix A. Based on the dimensionless variables introduced in Eq. (A.1), the rescaled free energy can be written as

$$\tilde{\mathcal{F}} = \frac{1}{2} \tilde{a}_2 \tilde{e}_2^2 - \frac{1}{4} \tilde{e}_2^4 + \frac{1}{6} \tilde{e}_2^6 + \frac{1}{2} \left(\frac{\partial \tilde{e}_2}{\partial \tilde{x}} \right)^2, \quad (\text{B.1})$$

with

$$e_c = \sqrt{\frac{a_4}{a_6}}, \quad \delta = \sqrt{\frac{k_g a_6}{a_4^2}}, \quad \tilde{a}_2 = \frac{a_2 a_6}{a_4^2} \frac{(\theta - \theta_m)}{\theta_m}, \quad \mathcal{F}_c = \delta^2 e_c^6 a_6. \quad (\text{B.2})$$

References

- [1] D. Lagoudas, Shape Memory Alloys: Modeling and Engineering Applications, Springer, London, 2008.
- [2] K. Bhattacharya, Microstructure of Martensite: Why it Forms and How it Gives Rise to the Shape-Memory Effect, Oxford University Press, 2003.
- [3] E. Patoor, D. Lagoudas, P. Entchev, L. Brinson, X. Gao, Mech. Mater. 38 (2006) 391–429.
- [4] A. Khandelwal, V. Buravalla, Int. J. Struct. Changes Solids – Mech. Appl. 1 (2009) 111–148.
- [5] L. Chen, Annu. Rev. Mater. Res. 32 (2002) 113–140.
- [6] L. Chen, J. Am. Ceram. Soc. 91 (2008) 1835–1844.
- [7] D. Seol, S. Hu, Y. Li, L. Chen, K. Oh, Mater. Sci. Forum 408 (2002) 1645–1650.
- [8] J. Zhang, Y. Li, D. Schlom, L. Chen, F. Zavaliche, R. Ramesh, Q. Jia, Appl. Phys. Lett. 90 (2007) 052909.
- [9] J. Slutsker, A. Antermev, A. Roytburd, Phys. Rev. Lett. 100 (2008) 087602.
- [10] A. Khachaturian, Theory of Structural Transformations in Solids, John Wiley and Sons, New York, NY, 1983.
- [11] A. Artemev, Y. Jin, A. Khachaturyan, Acta Mater. 49 (2001) 1165–1177.
- [12] R. Melnik, A. Roberts, K. Thomas, Proc. SPIE 3667 (1999) 290–301.
- [13] R. Melnik, A. Roberts, K.A. Thomas, Comput. Mater. Sci. 18 (2002) 255–268.
- [14] R. Ahluwalia, T. Lookman, A. Saxena, MRS Bull. 54 (2006) 2109–2120.
- [15] M. Bouville, R. Ahluwalia, Acta Mater. 56 (2008) 3558–3567.
- [16] A. Idesman, J. Cho, V. Levitas, Appl. Phys. Lett. 93 (2008) 043102.
- [17] V. Levitas, D. Preston, Phys. Rev. B 66 (2002) 134206.
- [18] S. Gadaj, W. Nowacki, E. Pieczyska, Infrared Phys. Technol. 43 (2002) 151–155.
- [19] E. Pieczyska, H. Tobushi, in: 10'th International Conference on Quantitative InfraRed Thermography, 2010, pp. 5–10.
- [20] E. Pieczyska, S. Gadaj, W. Nowacki, H. Tobushi, Exp. Mech. 46 (2006) 531–542.
- [21] R. Melnik, R. Mahapatra, Comput. Struct. 85 (2007) 698–711.
- [22] L. Wang, R. Melnik, Lect. Notes Comput. Sci. 3029 (2004) 645–652.
- [23] L. Wang, R. Melnik, Mater. Sci. Eng. A Struct. Mater. 438–440 (2006) 427–430.
- [24] T. Waitz, T. Antretter, F. Fischer, N. Simha, H. Karnthaler, Acta Mater. 55 (2007) 419–444.
- [25] A. Thompson, A. Strachan, Phys. Rev. B 81 (2009) 085429.
- [26] T. Waitz, K. Tsuchiya, T. Antretter, F. Fischer, MRS Bull. 34 (2009) 814–821.
- [27] M. Porta, T. Castan, P. Lloveras, T. Lookman, A. Saxena, S. Shenoy, Phys. Rev. B 79 (2009) 214117.
- [28] E. Eliseev, A. Morozovska, J. Mater. Sci. 44 (2009) 5149–5160.
- [29] C. Carstensen, Acta Numer. 5 (1996) 191–256.
- [30] C. Carstensen, Comput. Method Appl. Mech. Eng. 194 (2005) 169–193.
- [31] S. Müller, Variational Models for Microstructure and Phase Transitions: Calculus of Variations and Geometric Evolution Problems, Springer, 1999, pp. 85–210.
- [32] T. Lookman, S.R. Shenoy, K. Rasmussen, A. Saxena, A.R. Bishop, Phys. Rev. B Condens. Matter. Mater. Phys. 67 (2003) 24114.
- [33] L. Wang, R. Melnik, Appl. Numer. Math. 58 (2008) 511–524.
- [34] T. Lookman, P. Littlewood, MRS Bull. 34 (2009) 822–831.
- [35] R. Melnik, L. Wang, O. Tsviliuk, Proc. of SPIE, Behavior and Mechanics of Multifunctional Materials and Composites 7644 (2010) 1–10.
- [36] K. Rabe, C. Ahn, J. Triscone, Physics of Ferroelectrics: A Modern Perspective, Springer-Verlag, 2007.
- [37] J. Massad, R. Smith, J. Intell. Mater. Syst. Struct. 14 (2003) 455–471.
- [38] F. Falk, Acta Metallurgica 28 (1980) 1773–1780.
- [39] V. Levitas, Proc. 4th European Conference on Computational Mechanics (2010) 1–2.
- [40] V. Levitas, M. Javanbakht, Phys. Rev. Lett. 105 (2010) 105701.
- [41] M. Bouville, R. Ahluwalia, Phys. Rev. B 79 (2009) 094110.
- [42] A. Planes, P. Lloveras, T. Castán, A. Saxena, M. Porta, Continuum Mech. Thermodyn. (2011) 1–9.
- [43] R. Melnik, L. Wang, Int. Conf. on Computational Methods for Coupled Problems in Science and Engineering Coupled Problems, 2009, pp. 1–4.
- [44] L. Wang, R. Melnik, Mech. Adv. Mater. Struct. 14 (2007) 665–676.
- [45] L. Wang, R. Melnik, Mater. Sci. Eng. A Struct. Mater. 481–482 (2008) 190–193.
- [46] Y. Wang, J. Li, Acta Mater. 58 (2010) 1212–1235.
- [47] R. Melnik, A. Roberts, K.A. Thomas, Comput. Mech. 29 (2002) 16–26.
- [48] T. Bruce, Energy methods, in: Advanced Dynamics for Engineers, HRW Series in Mechanical Engineering, CBS College Publishing, 1984.
- [49] R.E. Miller, V.B. Shenoy, Nanotechnology 11 (2000) 139.
- [50] A. Ricci, A. Ricciardi, Sens. Actuat. A Phys. 159 (2010) 141–148.
- [51] P. Matus, R. Melnik, L. Wang, I. Rybak, Math. Comput. Simulat. 65 (2004) 489–509.
- [52] T. Waitz, V. Kazykhanov, H.P. Karnthaler, Acta Mater. 52 (2004) 137–147.
- [53] R. Kretschmer, K. Binder, Phys. Rev. B 20 (1979) 1065–1076.
- [54] Y. Wang, W. Zhong, P. Zhang, Solid State Commun. 90 (1994) 329–332.
- [55] Y. Zheng, C. Woo, B. Wang, J. Phys.: Condens. Matter 20 (2008) 135–216.
- [56] S. Li, J. Eastman, Z. Li, C. Foster, R. Newnham, L. Cross, Phys. Lett. A 212 (1996) 341–346.
- [57] J. Reddy, Energy Principles and Variational Methods in Applied Mechanics, Wiley Publications, 2002.
- [58] S. Curnoe, A. Jacobs, Phys. Rev. B 64 (2001) 064101.
- [59] L. Chen, J. Shen, Comput. Phys. Commun. 108 (1998) 147–158.
- [60] N. Bubner, Continuum Mech. Thermodyn. 8 (1996) 293–308.
- [61] N. Bubner, G. Mackin, R. Rogers, Comput. Mater. Sci. 18 (2000) 245–254.
- [62] M. Ben Jaber, H. Smaoui, P. Terriault, Smart Mater. Struct. 17 (2008) 045005.
- [63] D. Mahapatra, R. Melnik, Math. Comput. Simulat. 76 (2007) 141–148.
- [64] S. Kartha, J.A. Krumhansl, J.P. Sethna, L.K. Wickham, Phys. Rev. B Condens. Matter. 52 (1995) 803–822.
- [65] C.J. Austin, T. Hughes, Y. Bazilevs, Isogeometric Analysis: Toward Integration of CAD and FEA, John Wiley & Sons, 2009.